Article

Five 2,6-Di(pyrazol-1-yl)pyridine-4-carboxylate Esters, and the Spin States of their Iron(II) Complexes

Iurii Galadzhun, Rafal Kulmaczewski, and Malcolm A. Halcrow *

School of Chemistry, University of Leeds, Woodhouse Lane, Leeds LS2 9JT, UK; cmig@leeds.ac.uk（I.G.）;
r.kulmaczewski@leeds.ac.uk (R.K.)

* Correspondence: m.a.halcrow@leeds.ac.uk; Tel.: +44-113-343-6506; Fax: +44-113-343-6565;

Abstract: Two phenyl ester and three benzyl ester derivatives have been synthesized from 2,6-di(pyrazol-1-yl)pyridine-4-carboxylic acid and the appropriate phenyl or benzyl alcohol using *N,N′*-dicyclohexylcarbodiimide as the coupling reagent. Complexation of the ligands with $Fe[BF_4]_2 \cdot 6H_2O$ in acetone yielded the corresponding $[FeL_2][BF_4]_2$ complex salts. Four of the new ligands and four of the complexes have been crystallographically characterised. Particularly noteworthy are two polymorphs of $[Fe(L^3)_2][BF_4]_2 \cdot 2MeNO_2$ (L^3 = 3,4-dimethoxyphenyl 2,6-di{pyrazol-1-yl}pyridine-4-carboxylate), one of which is crystallographically characterised as high-spin while the other exhibits the onset of spin-crossover above room temperature. The other complexes are similarly low-spin at low temperature but exhibit gradual spin-crossover on heating, except for an acetone solvate of $[Fe(L^5)_2][BF_4]_2$ (L^5 = benzyl 2,6-di{pyrazol-1-yl}pyridine-4-carboxylate), which exhibits a more abrupt spin-transition at $T_{1/2}$ = 273 K with 9 K thermal hysteresis.

Keywords: iron; N-donor ligand; spin-crossover; crystal structure; magnetic measurements

1. Introduction

Spin-crossover (SCO) compounds are an important class of molecular switches which are widely studied in molecular materials chemistry [1–3]. The SCO switching event changes a number of physical properties in a material including its colour, magnetic moment [4], volume [5], dielectric properties [6–9], conductivity [9–12], and fluorescence [13–15]. Solid or mesophase phase transitions and isotropic melting can also be coupled to spin transitions in soft materials containing SCO centres [16,17]. Moreover, a material's SCO switching properties are preserved at the nanoscale in particles [18] or thin films [19] above 30–50 nm in diameter (size effects become important at smaller length scales) [20]. This has led to SCO centres being incorporated into a variety of functional and multifunctional materials and prototype devices [3,21]. A popular family of compounds in spin-crossover (SCO) research is derived from $[Fe(bpp)_2]^{2+}$ (bpp = 2,6-di{pyrazol-1-yl}pyridine) [22–24]. Many functional groups can be appended to the bpp ligand skeleton [25], with predictable consequences for the spin state of the coordinated iron atom [26,27]. This flexibility has allowed emissive [28–31], photo-isomerizable [32], redox active [33,34], magnetically active [35,36]， and metal-binding substituents [31,37–39] as well as surface-binding tether groups [40–42] to be attached to the $[Fe(bpp)_2]^{2+}$ framework， giving a variety of multifunctional SCO molecular switches.

With that in mind， we [43] and others [29,35,36,44–46] have employed 2,6-di(pyrazol-1-yl)-pyridine-4-dicarboxylic acid [47] as a convenient precursor to new bpp derivatives bearing tether groups or other functionalities for SCO research. On our part, we recently reported a family of 2,6-di(pyrazol-1-yl)pyridine-4-dicarboxylate esters bearing long chain 4-alkoxyphenyl substituents,

which are derived from L^1 and L^2 (Scheme 1). The iron(II) complexes of these (potentially amphiphilic) ligands proved to have a varied structural chemistry that depends on the R^1 alkoxy chain length. Most of the compounds were low-spin around room temperature but underwent SCO on heating. Annealing at higher temperatures led to the loss of crystallinity, possibly from disordering of the alkoxy chain conformations, which had a strong effect on the metal spin state when the sample was recooled [43].


R^1 = OMe, L^1
R^1 = OH, L^2

R^2 = OMe, L^3
R^2 = OH, L^4

R^3 = H, L^5
R^3 = OMe, L^6

L^7
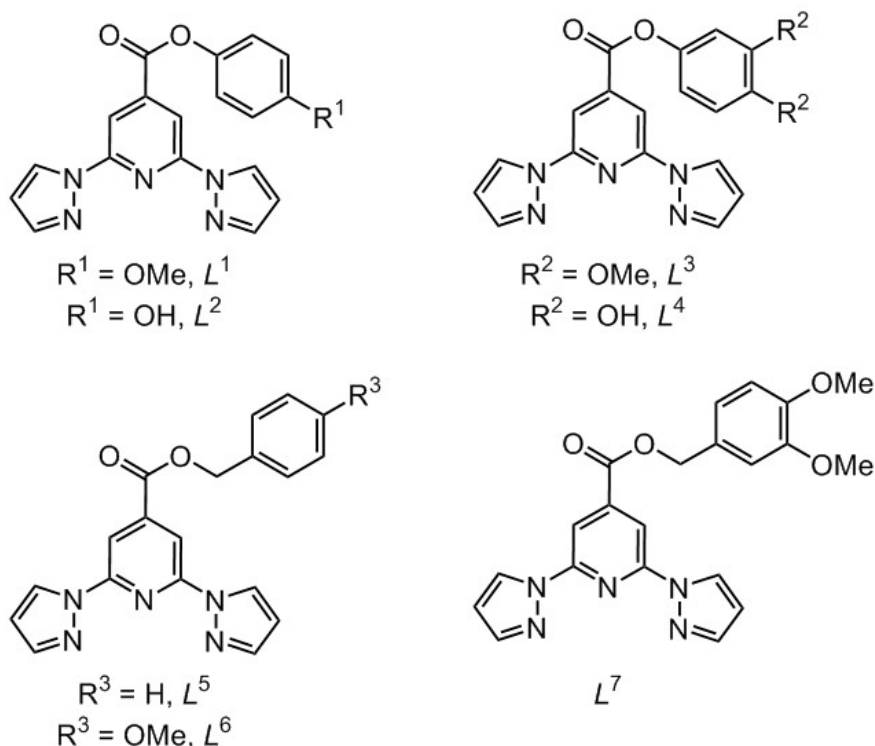
Scheme 1. Ligands referred to in this work. L^1, L^2 and their iron(II) complexes are described in [43].

As a continuation of this work, we describe two new series of 2,6-di(pyrazol-1-yl)pyridine-4-dicarboxylate esters and their iron complex chemistry. First are two dimethoxy or dihydroxyphenyl esters L^3 and L^4 as models for new derivatives bearing two R^2 alkoxy chains per ligand, which may increase their amphiphilic character. Second are the first three benzyl 2,6-di(pyrazol-1-yl)pyridine-4-dicarboxylate esters L^5–L^7 to examine how additional conformational flexibility in the ester linkage affects the structural chemistry of this family of compounds.

2. Results and Discussion

2.1. Synthesis

2,6-Di(pyrazol-1-yl)pyridine-4-carboxylic acid was prepared by the literature route, from pyrazole and 2,6-dibromopyridine-4-dicarboxylic acid (Scheme 2) [47]. Refluxing this precursor in thionyl chloride converted it in situ to 2,6-di(pyrazol-1-yl)pyridine-4-carbonyl chloride, which was then treated with 3,4-dimethoxyphenol to afford L^3 in 55% overall yield. Conversion of L^3 to L^4 was achieved in 69 % yield using a ten-fold excess of boron tribromide. Alternatively, reaction of 2,6-di(pyrazol-1-yl)pyridine-4-carboxylic acid with the appropriate benzyl alcohol, in the presence of the coupling agent *N,N*-dicyclohexyl carbodiimide (DCC) and catalytic 4-(dimethylamino)pyridine (DMAP), gave L^5–L^7 in low-to-moderate recrystallized yields. The identities of all the ligands were confirmed by ^{1}H and ^{13}C NMR and HR-ESMS spectrometry, while four of the new ligands were also characterised by *X*-Ray crystallography.
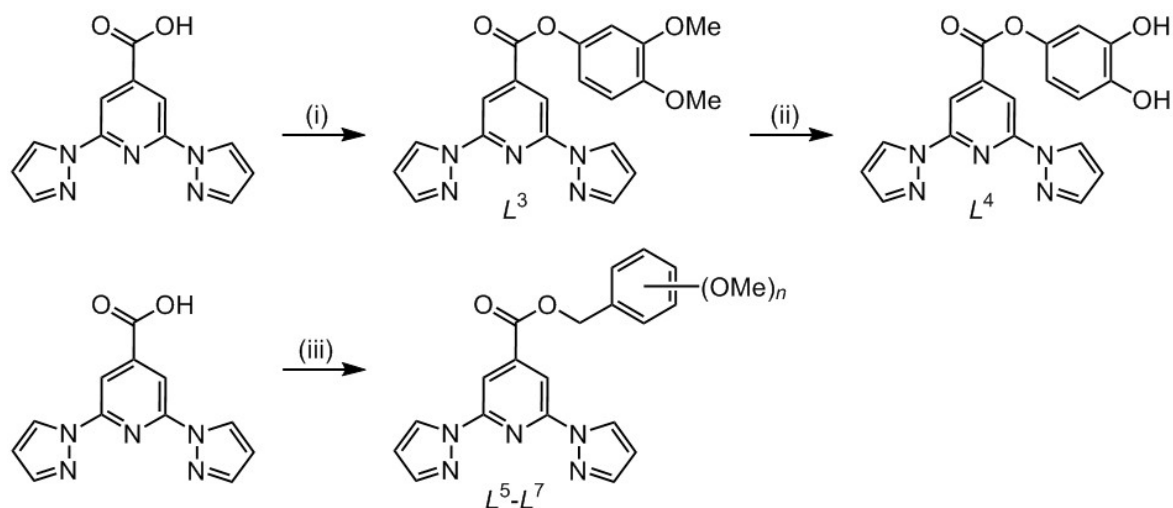
Scheme 2. Syntheses of the new ligands. Reagents and conditions: (i) $SOCl_2$, reflux, 12 hr then 3,4-dimethoxyphenol, dimethylformamide, NEt_3, rt, 48 hr. (ii) BBr_3, CH_2Cl_2, −78 °C → reflux, 4 hr. (iii) Benzyl alcohol, *N,N*-dicyclohexyl carbodiimide, DMAP (cat), dichloromethane, rt, 48 hr.

The salts [Fe*L*$_2$][BF$_4$]$_2$ (*L*^{3}–*L*^{7}) were obtained by complexing 0.5 equiv of Fe[BF$_4$]$_2$·6H$_2$O by the appropriate ligand in acetone, which yielded the products as red or brown microcrystals after the usual work-up. All the complexes were solvent-free solids by microanalysis after drying in vacuo, except [Fe(*L*^{4})$_2$][BF$_4$]$_2$, which contained 2 equiv lattice water. While this solvent is not evident in the crystal structure of that complex, the disorder in the crystal (see below) and the hydrogen bonding capabilities of the *L*^{4} ligand could both facilitate absorption of atmospheric moisture by the bulk material.
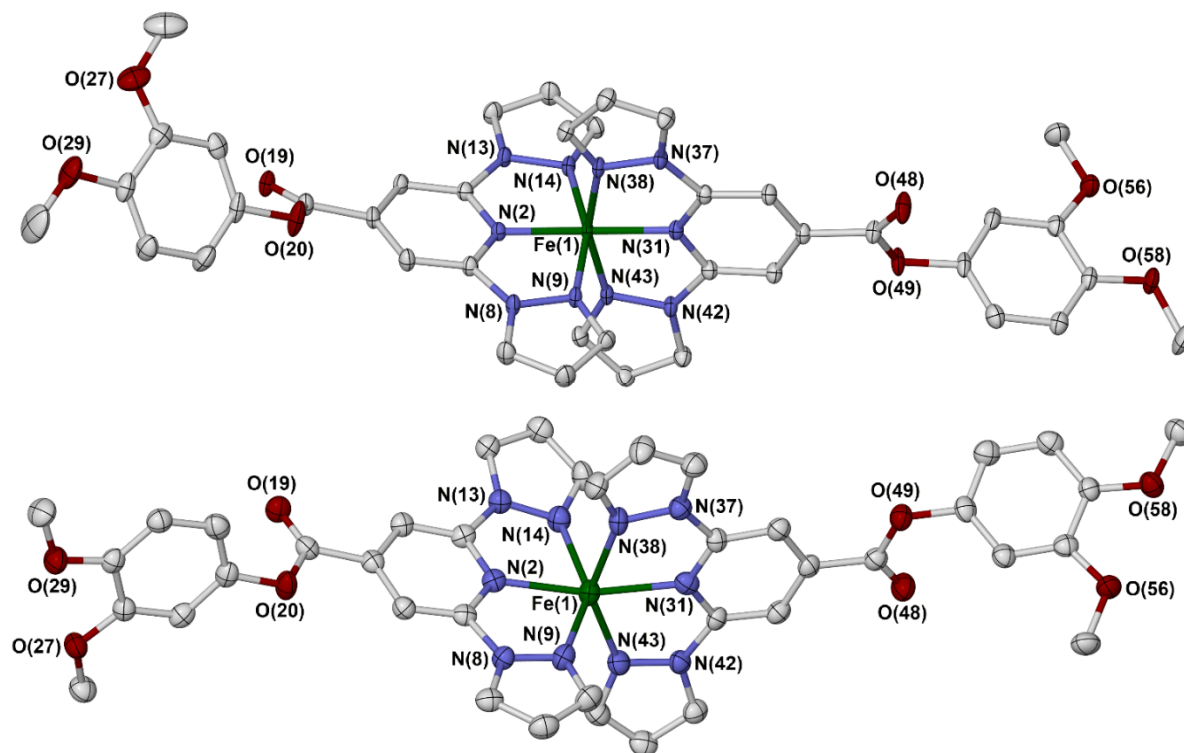
2.2. Crystallographic Characterization

All the new ligands except *L*^{4} were crystallographically characterised. The pyridyl and pyrazolyl groups in the *tris*-heterocyclic ligand cores all adopt the *anti*-coplanar orientation that is typically found in crystalline bpp derivatives [48]. This avoids repulsive interactions between the pyridyl *N*1 and pyrazolyl *N*2 lone pairs [49]. The asymmetric units of *L*^{5} and *L*^{7}·½MeCN both contain two crystallographically independent ligand molecules (*ie* *Z*′ = 2). While the two unique molecules of *L*^{5} have essentially identical conformations, the two molecules of *L*^{7} show significantly different torsions about their benzyl substituent methylene groups.

Recrystallization of [Fe(*L*^{3})$_2$][BF$_4$]$_2$ from nitromethane/diethyl ether gave mixtures of two crystal forms, which were readily distinguished by their dark red and bright yellow colouration and proved to be polymorphs of formula [Fe(*L*^{3})$_2$][BF$_4$]$_2$·2MeNO$_2$ (Figure 1). Both polymorphs exhibit the triclinic space group $P\bar{1}$ but with significantly different unit cell parameters. Crystals of the major red α-polymorph are low-spin at 120 K according to the metric parameters at the iron atom, while the minor yellow β-polymorph is high-spin at the same temperature (Table 1). As well as the expanded FeN$_6$ coordination sphere expected for a high-spin complex [50], the coordination geometry of the β-polymorph is significantly more distorted away from the idealized D_{2d} symmetry expected for this ligand combination. This is evident in the *trans*-N{pyridyl}–Fe–N{pyridyl} angle (ϕ), and the dihedral angle between the least squares planes of the heterocyclic cores of the two *L*^{3} ligands (θ). Both parameters in the α-polymorph are close to their idealized values of 180 and 90°, respectively (Table 1), which is to be expected in low-spin [Fe(bpp)$_2$]$^{2+}$ derivatives [22]. However, the β-polymorph exhibits reduced values of $\phi = 166.41(12)°$ and $\theta = 79.90(3)°$. Deviations of these parameters from their ideal values are common in high-spin compounds [24] and reflect an angular Jahn–Teller distortion of the high-spin ^5T configuration [51,52]. Since the distortion is only a property of the high-spin molecules, distorted molecules must rearrange to a more regular coordination geometry during spin-crossover, which can be inhibited in a rigid solid lattice. In practice, spin-crossover is rarer in complexes exhibiting $\phi < 172°$ in their high-spin form, as in β-[Fe(*L*^{3})$_2$][BF$_4$]$_2$·2MeNO$_2$ [53].

Table 1 Metric parameters for the two polymorphs of $[Fe(L^3)_2][BF_4]_2\cdot 2MeNO_2$ (Å, Å³, º). V_{Oh}, Σ, and Θ are indices characteristic for the spin state of the complex [50,54], while θ and ϕ are defined in the text [50]. Typical values of these parameters in $[Fe(bpp)_2]^{2+}$ derivatives are given in [22] and [55].

	α-$[Fe(L^3)_2][BF_4]_2\cdot 2MeNO_2$	β-$[Fe(L^3)_2][BF_4]_2\cdot 2MeNO_2$
Fe−N{pyridyl}	1.8903(17), 1.8917(17)	2.143(3), 2.156(4)
Fe−N{pyrazolyl}	1.9502(19)−1.9831(19)	2.151(3)−2.208(4)
V_{Oh}	9.446(5)	12.357(13)
Σ	84.6(3)	159.2(4)
Θ	275	475
ϕ	174.29(8)	166.41(12)
θ	89.79(2)	79.90(3)

Figure 1. View of the complex dications in the low-spin α-polymorph (top) and high-spin β-polymorph (bottom) of β-$[Fe(L^3)_2][BF_4]_2\cdot 2MeNO_2$. Displacement ellipsoids are at the 50% probability level, and H atoms are omitted. Colour code: C, white; Fe, green; N, blue; O, red.

Solvent-free crystals of $[Fe(L^4)_2][BF_4]_2$, and acetonitrile solvates of $[Fe(L^5)_2][BF_4]_2$ and $[Fe(L^6)_2][BF_4]_2$ were also crystallographically characterised. While not being isostructural, all three of these compounds contain two unique complex molecule environments in their asymmetric units (i.e., $Z' = 2$). Both complex cations in each compound are low-spin at 120 K, with only minor differences in their coordination geometries (Table 2). Most notable is molecule B in $[Fe(L^6)_2][BF_4]_2\cdot{}^3/_2MeCN$, whose inter-ligand dihedral angle $[\theta = 83.18(4)°]$ is at the low end of the usual range for a low-spin $[Fe(bpp)_2]^{2+}$ derivative [22]. This reflects a distorted conformation in ligand N(2B)-C(29B) caused by two short intermolecular C–H…π contacts involving benzylic CH_2 groups in the lattice (Figure 2).

The two unique molecules in each crystal differ in the disposition of their ester substituents. One dihydroxyphenyl group in molecule B of $[Fe(L^4)_2][BF_4]_2$ is badly disordered, reflecting a steric clash with its symmetry equivalent across a crystallographic inversion centre (Figure 3). The disorder extends to two BF_4^- ions (and their symmetry equivalents) which hydrogen bond to this dihydroxy-phenyl residue. The two cations in $[Fe(L^5)_2][BF_4]_2\cdot{}^3/_2MeCN$ (Figure 4) and $[Fe(L^6)_2][BF_4]_2\cdot{}^3/_2MeCN$ show less dramatic ligand disorder but have different torsions about their benzylic methylene groups.

Table 2 Metric parameters for the other crystallographically characterised complexes (Å, Å³, º).

Compound	[Fe(L⁴)₂][BF₄]₂		[Fe(L⁵)₂][BF₄]₂·³/2MeCN	
Molecule	**Molecule A**	**Molecule B**	**Molecule A**	**Molecule B**
Fe−N{pyridyl}	1.897(3), 1.897(3)	1.888(3), 1.898(3)	1.892(2), 1.892(2)	1.890(2), 1.891(2)
Fe−N{pyrazolyl}	1.956(4)−1.990(4)	1.965(4)−1.977(4)	1.955(2)−1.964(3)	1.953(3)−1.972(3)
V_{Oh}	9.537(11)	9.499(11)	9.392(7)	9.405(8)
V_{Oh}	88.8(5)	84.8(5)	84.3(4)	83.6(4)
Σ	275	278	276	274
Θ	176.93(16)	178.09(16)	175.96(11)	178.45(11)
ϕ	85.54(5)	87.63(4)	88.14(3)	87.78(3)

Compound	[Fe(L⁶)₂][BF₄]₂·³/2MeCN	
Molecule	**Molecule A**	**Molecule B**
Fe−N{pyridyl}	1.889(3), 1.896(3)	1.891(3), 1.897(3)
Fe− N{pyrazolyl}	1.965(4)−1.978(3)	1.963(4)−1.996(4)
V_{Oh}	9.501(10)	9.538(11)
Σ	83.7(5)	90.5(5)
Θ	277	274
ϕ	176.34(15)	175.93(15)
θ	89.77(3)	83.18(4)
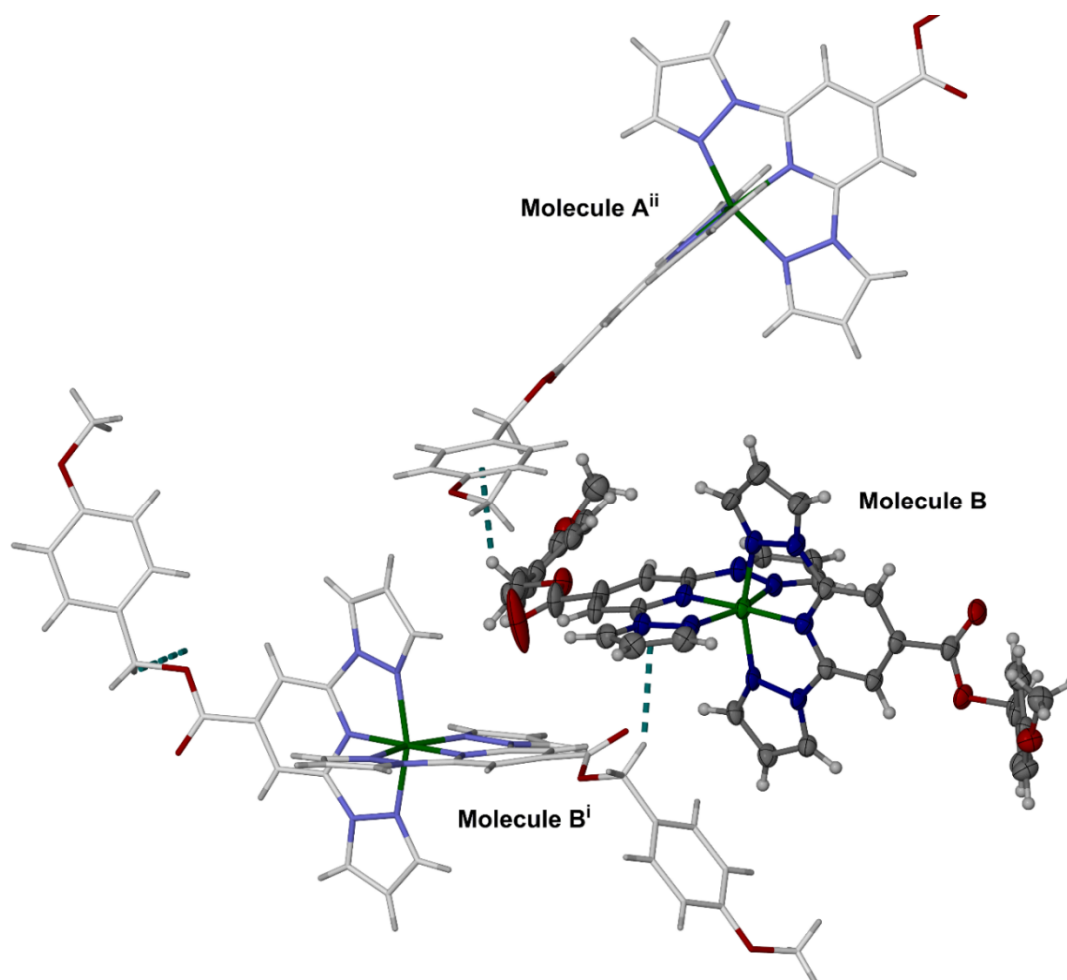
Figure 2. Intermolecular C–H…π interactions causing the twisted ligand conformation in molecule 'B' of [Fe(L⁶)₂][BF₄]₂·³/2MeCN, which is highlighted with dark colouration. Symmetry codes: (i) *x*, ³/2–*y*, ¹/2+*z*; (ii) 1–*x*, 1–*y*, 1–*z*. Colour code: C, white or dark grey; H, pale grey; Fe, green; N, pale or dark blue; O, red.
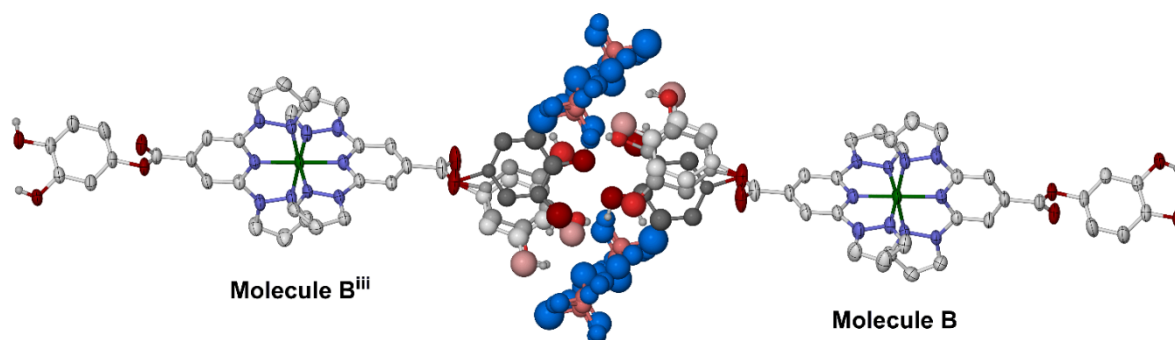
Figure 3. Ligand and anion disorder about a crystallographic inversion centre in molecule 'B' of $[Fe(L^4)_2][BF_4]_2$. C-bound H atoms are omitted for clarity; other details as for Figure 1. The three disorder sites of the dihydroxyphenyl substituents are distinguished with pale, medium, and dark colouration. Symmetry code: (iii) –*x*, 2–*y*, –*z*. Colour code: C, white, pale or dark grey; H, pale grey; B, pink; F, cyan; Fe, green; N, blue; O, pale, medium, or dark red.
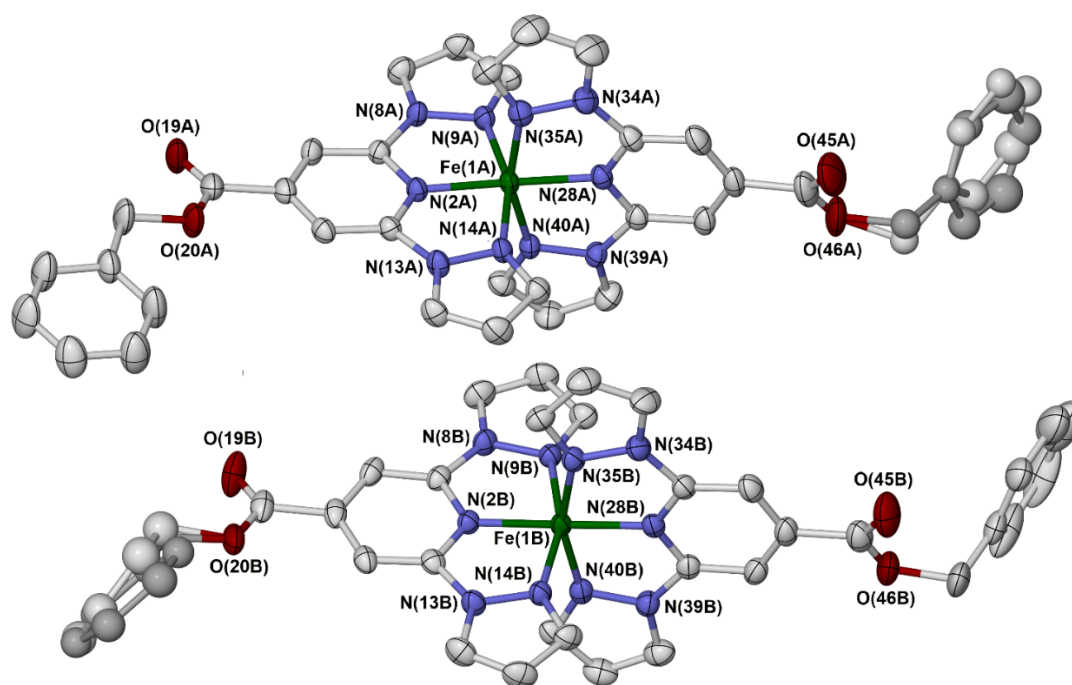

Figure 4. The complex dications in $[Fe(L^5)_2][BF_4]_2 \cdot 3/2MeCN$, showing the orientations of their benzyl substituents. Benzyl group disorder sites are distinguished with pale and dark colouration. Other details as for Figure 1. Colour code: C, white or grey; Fe, green; N, blue; O, red.

Lastly, a preliminary structure solution was achieved from a weakly diffracting crystal of $[Fe(L^7)_2][BF_4]_2 \cdot nMe_2CO \cdot \frac{1}{4}H_2O$ (orthorhombic, space group *Pna*2_1), which was also clearly low-spin at 120 K. Interestingly, this crystal also has *Z*′ = 2, with two unique complex molecules in its asymmetric unit. Although a full refinement of that structure was not achieved, the preliminary model was sufficient to compare with the powder diffraction data from that compound as described below.

2.3. Characterization of the Bulk Materials

The freshly prepared $[Fe(L^3)_2][BF_4]_2 \cdot 2MeNO_2$ was a mixture of the *α*- and *β*-polymorphs, but the pure *α*-polymorph could be obtained by decanting off crystals of the *β*-form. X-Ray powder diffraction data from *α*-$[Fe(L^3)_2][BF_4]_2 \cdot 2MeNO_2$, $[Fe(L^4)_2][BF_4]_2$, and $[Fe(L^7)_2][BF_4]_2 \cdot nMe_2CO \cdot \frac{1}{4}H_2O$ at 298 K showed good agreement with their crystallographic simulations (Figure 5). Hence, these compounds retain their structural integrity on exposure to air, despite the tendency of $[Fe(L^4)_2][BF_4]_2$ to absorb atmospheric moisture. However, $[Fe(L^5)_2][BF_4]_2 \cdot 3/2MeCN$ and $[Fe(L^6)_2][BF_4]_2 \cdot 3/2MeCN$

exhibited additional diffraction peaks on top of their crystallographically characterised phases, which may reflect structural changes during solvent loss from those materials under ambient conditions.
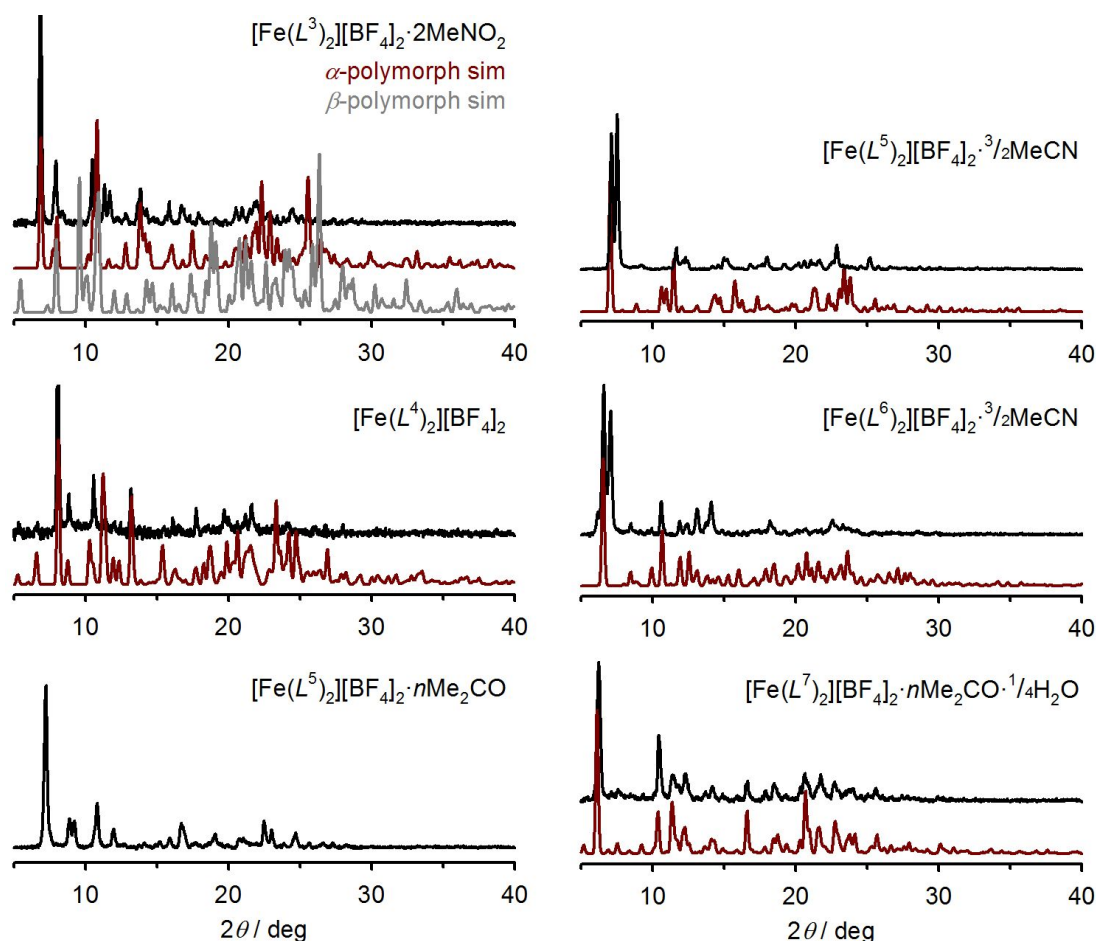
Figure 5. Measured (black) and simulated (red, grey) X-Ray powder diffraction data from the complexes in this work. No crystallographic simulation is available for [Fe(L^5)$_2$][BF$_4$]$_2$·nMe$_2$CO.

Magnetic susceptibility data from freshly prepared [Fe(L^3)$_2$][BF$_4$]$_2$·2MeNO$_2$ showed a constant $\chi_M T$ value of 1.1 cm^3 mol^{-1} K between 50–100 K (where zero-field splitting effects do not operate), implying a ca. 30 % high-spin population at those temperatures (Figure 6). That is consistent with a mixture of low-spin α- and high-spin β-polymorphs, as observed crystallographically. A gradual increase in $\chi_M T$ on further warming may imply the onset of SCO in α-form at higher temperatures. This was confirmed by measurement of the purified α-polymorph of the complex, which is diamagnetic and fully low-spin below 220 K but shows a gradual increase in $\chi_M T$ on further heating, reaching 0.7 cm^3 mol^{-1} K at 350 K. That is consistent with high-temperature SCO, with $T_{1/2} > 400$ K, from extrapolation of the data. This resembles other [Fe(bpp)$_2$]$^{2+}$ complex salts bearing carboxy substituents, which often exhibit SCO significantly above room temperature in the solid state [27,36,43–46].

Magnetic data from most of the other complexes are similar in being low-spin below 150 K (in agreement with their crystal structures) while undergoing gradual SCO with $T_{1/2} \geq 350$ K. However, [Fe(L^4)$_2$][BF$_4$]$_2$ shows a low-temperature $\chi_M T$ value of 1.6 cm^3 mol^{-1} K between 50–100 K, implying almost 50% of the sample remains high-spin at all temperatures, which is inconsistent with its crystallographic data (Table 2). While the sample was phase pure by powder diffraction (Figure 5), it also contained lattice water by microanalysis, which is not evident in the crystal structure. That may indicate the presence of an amorphous, possibly hydrated, high-spin fraction in the material.
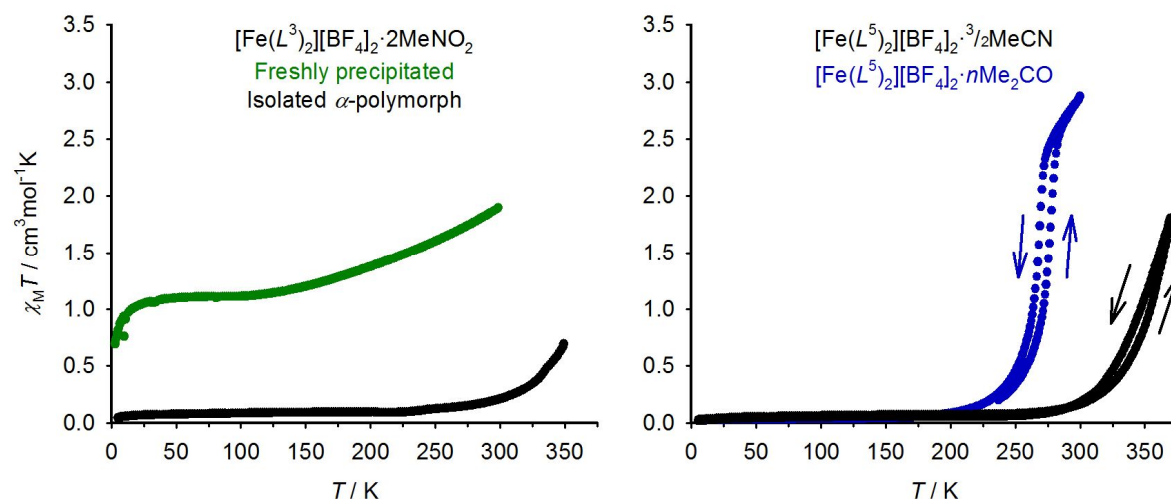
Figure 6. Variable temperature magnetic susceptibility data for different preparations of [Fe(*L*³)₂][BF₄]₂·2MeNO₂ (left) and [Fe(*L*⁵)₂][BF₄]₂ (right), at a scan rate of 5 K min⁻¹. Data for [Fe(*L*³)₂][BF₄]₂·2MeNO₂ were measured on a cooling temperature ramp only.

The other noteworthy material is [Fe(*L*⁵)₂][BF₄]₂, which was obtained in two different, presumably solvated forms. Crystallographically characterised [Fe(*L*⁵)₂][BF₄]₂·3/2MeCN exhibits the expected SCO above room temperature with $T_{1/2}$ = 370 K (Figure 6). The SCO is monotonic within the temperature range of the measurement, showing the two unique molecular environments in the crystal undergo SCO at similar temperatures. The transition is also reversible with a narrow thermal hysteresis, implying it is barely perturbed by any solvent loss when the sample is heated. However, after recrystallization from acetone/diethyl ether, the same complex showed a more abrupt, hysteretic spin-transition centred just below room temperature ($T_{1/2}\downarrow$ = 269 K, $T_{1/2}\uparrow$ = 278 K at a scan rate of 5 K min⁻¹). This phase is not isostructural with the MeCN solvate (Figure 5), but since its crystals were unsuitable for a crystallographic determination, the structural origin of this enhanced SCO cooperativity is presently unclear.

SCO in [Fe(*L*³)₂][BF₄]₂ and [Fe(*L*⁴)₂][BF₄]₂ was also measured in CD₃CN solution by the Evans method, which demonstrated almost complete SCO equilibria for both compounds over the liquid range of the solvent (Figure 7). Thermodynamic parameters and spin-crossover midpoint temperatures were derived from these data by fitting these data to equations 1 and 2, where *n*HS(*T*) is the high-spin fraction of the sample at temperature *T*:
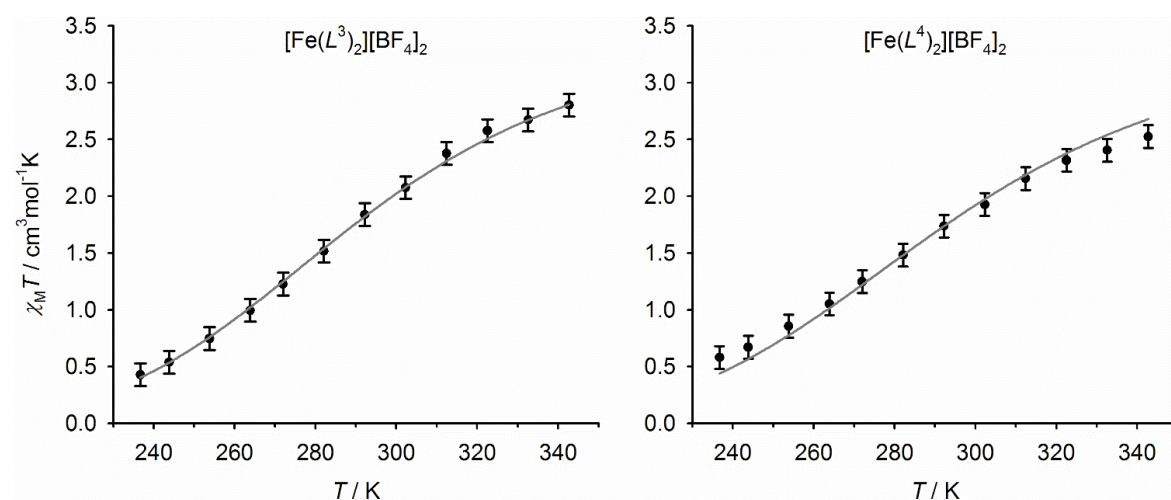
Figure 7. Magnetic susceptibility data for [Fe(*L*³)₂][BF₄]₂ (left) and [Fe(*L*⁴)₂][BF₄]₂ (right) in CD₃CN solution. The lines show the fits of the data to equations 1 and 2.

$$\ln[(1 - n\text{HS}(T))/n\text{HS}(T)] = \Delta H/RT - \Delta S/R \tag{1}$$

$$\Delta S = \Delta H/T_{\frac{1}{2}} \tag{2}$$

The fitted parameters were $T_{\frac{1}{2}}$ = 289.2(4) K, ΔH = 22.0(3) kJ mol^{-1}, ΔS = 76(2) J mol^{-1} K^{-1} for [Fe(L^3)$_2$][BF$_4$]$_2$; and $T_{\frac{1}{2}}$ = 292(1) K, ΔH = 20(1) kJ mol^{-1}, ΔS = 68(3) J mol^{-1} K^{-1} for [Fe(L^4)$_2$][BF$_4$]$_2$. These values resemble those of [Fe(L^1)$_2$][BF$_4$]$_2$ and [Fe(L^2)$_2$][BF$_4$]$_2$ in the same solvent [43] and show the hydrogen bonding capability of L^4 has little effect on the spin state of its iron complex. While the lower entropy of SCO for [Fe(L^4)$_2$][BF$_4$]$_2$ could reflect a more rigid, hydrogen bonded solvent shell around that complex, this is uncertain since the difference between the two compounds is close to the error of the measurement.

3. Experimental Section

3.1. Instrumentation

Elemental microanalyses were performed by the microanalytical services at the University of Leeds School of Chemistry, or the London Metropolitan University School of Human Sciences. Electrospray mass spectra were recorded on a Bruker MicroTOF-q instrument from CHCl$_3$ solution. Diamagnetic NMR spectra employed a Bruker Ascend Advance III spectrometer operating at 400.1 MHz (^{1}H) or 100.6 MHz (^{13}C), while paramagnetic ^{1}H NMR spectra were obtained with a Bruker DPX300 spectrometer operating at 300.1 MHz. X-Ray powder diffraction measurements were obtained from a Bruker D2 Phaser diffractometer, using Cu-K_α radiation (λ = 1.5419 Å).

Magnetic susceptibility measurements were performed using a Quantum Design VSM SQUID magnetometer in an applied field of 5000 G with a temperature ramp of 5 K min^{-1}. Diamagnetic corrections for the samples were estimated from Pascal's constants [56], and SCO $T_{\frac{1}{2}}$ values were estimated as the temperature where $\chi_M T$ = 1.75 cm^3 mol^{-1} K (high-spin complexes of this type typically exhibit $\chi_M T$ = 3.5 ± 0.1 cm^3 mol^{-1} K [22]). Susceptibility measurements in solution were obtained by Evans method using a Bruker Avance 500 FT spectrometer operating at 500.1 MHz [57,58]. A diamagnetic correction for the sample [56], and a correction for the variation of the density of the CD$_3$CN solvent with temperature [59], were applied to these data.

3.2. Synthesis

2,6-Di(pyrazol-1-yl)pyridine-4-carboxylic acid (bpp$^{\text{COOH}}$) was prepared by the literature method [47].

3.2.1. Synthesis of 3,4-dimethoxyphenyl 2,6-di(pyrazol-1-yl)pyridine-4-carboxylate (L^3)

A mixture of bpp$^{\text{COOH}}$ (1.28 g, 5.0 mmol) and thionyl chloride (10 cm^3) was heated at reflux for 12 hr. The coloured solution was evaporated to dryness, and the resultant 2,6-di(pyrazol-1-yl)pyridine-4-carbonyl chloride was redissolved in dimethylformamide (DMF, 15 cm^3). A mixture of 3,4-dimethoxyphenol (0.77 g, 5.0 mmol) and triethylamine (20 cm^3) in DMF (10 cm^3) was added to this solution. The reaction was stirred for 48 hr at room temperature, yielding a large quantity of precipitate. Water (40 cm^3) was added to the stirred reaction mixture, which precipitated the product as an off-white solid. The product was collected, washed with water, and dried in vacuo. Yield: 1.08 g, 55%. Mp: 201–202 °C. HR-ES MS m/z 392.1387 (calculated for [(C$_{20}$H$_{17}$N$_5$O$_4$)H]$^+$ 392.1353). ^{1}H NMR ({CD$_3$}$_2$SO) δ 3.77, 3.79 (both s, 3H, OCH_3), 6.70 (dd, 1.7 and 2.4 Hz, 2H, Pz H^4), 6.89 (dd, 1H, Ph H^6), 7.03 (d, 1H, Ph H^5), 7.08 (d, 1H, Ph H^2), 7.94 (d, 2H, Pz H^3), 8.31 (s, 2H, Py $H^{3/5}$), 9.04 (d, 2H, Pz H^5). ^{13}C NMR ({CD$_3$}$_2$SO) δ 55.8, 55.9 (both 1C, OCH$_3$), 106.3 (1C, Ph C^2), 108.2 (2C, Py $C^{3/5}$), 109.1 (2C, Pz C^4), 111.8 (1C, Ph C^6), 112.9 (1C, Ph C^5), 128.5 (2C, Pz C^5), 142.7 (1C, Ph C^3), 143.4 (2C, Pz C^3), 143.8 (1C, Py C^4), 147.0 (1C, Ph C^4), 149.3 (1C, Ph C^1), 150.5 (2C, Py $C^{2/6}$), 162.7 (1C, COOR).

3.2.2. Synthesis of 3,4-dihydroxyphenyl 2,6-di(pyrazol-1-yl)pyridine-4-carboxylate (L^4)

L^3 (1.56 g, 4 mmol) was dissolved in dry dichloromethane (40 cm³) under nitrogen. The reaction mixture was cooled to –78 °C, and boron tribromide (4 cm³, 42.2 mmol) was added dropwise. The stirred solution was then heated to reflux for 4 hr, yielding an orange solution which was cooled in ice water. Water (20 cm³) was added dropwise to the solution, and red and white precipitates were collected separately, washed with water, dried on the filter, then washed with dichloromethane. Recrystallization of the two solids from acetone in each case yielded off-white powders, which proved to be the same compound L^4 by ¹H NMR. Yield: 1.01 g, 69%. Mp: 257–258 °C. HR-ES MS *m/z* 364.1041 (calculatedd for [(C₁₈H₁₃N₅O₄)H]⁺ 364.0991), 386.0865 (calculated for [(C₁₈H₁₃N₅O₄)Na]⁺ 386.0860). ¹H NMR ({CD₃}₂SO) δ 6.64 (dd, 1H, Ph *H⁶*), 6.71 (pseudo-t, 2H, Pz *H⁴*), 6.77 (d, 1H, Ph *H²*), 6.82 (d, 1H, Ph *H⁵*), 7.95 (d, 2H, Pz *H³*), 8.29 (s, 2H, Py *H³/⁵*), 9.04 (d, 2H, Pz *H⁵*), 9.34 (br s, 2H, O*H*). ¹³C NMR ({CD₃}₂SO) δ 108.2 (2C, Py *C³/⁵*), 109.0 (2C, Pz *C⁴*), 109.3 (1C, Ph *C²*), 111.6 (1C, Ph *C⁶*), 115.3 (1C, Ph *C⁵*), 128.5 (2C, Pz *C⁵*), 142.4 (1C, Ph *C³*), 142.8 (1C, Py *C⁴*), 143.4 (2C, Pz *C³*), 147.0 (1C, Ph *C⁴*), 145.8 (1C, Ph *C¹*), 150.5 (2C, Py *C²/⁶*), 162.7 (1C, *C*OOR).

3.2.3. Synthesis of benzyl 2,6-di(pyrazol-1-yl)pyridine-4-carboxylate (L⁵)

A mixture of bpp^COOH (1.00 g, 3.92 mmol), *N,N*-dicyclohexyl carbodiimide (DCC; 1.78 g, 8.62 mmol), benzyl alcohol (0.42 g (3.92 mmol), and a catalytic amount of dimethylaminopyridine (DMAP) in dichloromethane (50 cm³) was stirred for 2 days under a CaCl₂ tube. The resultant precipitate was removed, and the yellow filtrate was evaporated to dryness. Recrystallization of the solid residue from acetonitrile/ethyl acetate yielded an almost pure compound, which was further purified by a short silica chromatography column (1:1 hexane:ethyl acetate eluent) which yielded the product as colourless plate-like crystals. Yield: 0.25 g, 19%. Mp: 120–121 °C. HR-ES MS *m/z* 346.1302 (calculated for [(C₁₉H₁₅N₅O₂)H]⁺ 346.1299), 368.1130 (calculated for [(C₁₉H₁₅N₅O₂)Na]⁺ 368.1118). ¹H NMR (CDCl₃) δ 5.44 (s, 2H, C*H₂*), 6.52 (pseudo-t, 2H, Pz *H⁴*), 7.39 (m, 2H, Ph *H²/⁶*), 7.48 (m, 3H, Ph *H³⁻⁵*), 7.79 (d, 2H, Pz *H³*), 8.41 (s, 2H, Py *H³/⁵*), 8.56 (d, 2H, Pz *H⁵*). ¹³C NMR (CDCl₃) δ 68.0 (1C, *C*H₂), 108.6 (2C, Pz *C⁴*), 109.4 (2C, Py *C³/⁵*), 127.4 (2C, Pz *C⁵*), 128.8 (2C, Ph *C³/⁵*), 128.9 (1C, Ph *C⁴*), 128.9 (2C, Ph *C²/⁶*), 135.3 (1C, Ph *C¹*), 143.0 (2C, Pz *C³*), 143.5 (1C, Py *C⁴*), 145.8 (1C, Ph *C¹*), 151.0 (2C, Py *C²/⁶*), 164.1 (1C, *C*OOR).

3.2.4. Synthesis of 4-methoxybenzyl 2,6-di(pyrazol-1-yl)pyridine-4-carboxylate (L⁶)

Method was as for L^5 using 4-methoxybenzyl alcohol (0.54 g, 3.92 mmol). The crude product from the initial reaction mixture was purified by flash silica column chromatography (1:1 hexane:ethyl acetate eluent) and obtained as a white crystalline powder. Yield: 0.22 g, 15%. Mp**:** 151–153 °C. HR-ES MS *m/z* 376.1402 (calculated for [(C₂₀H₁₇N₅O₃)H]⁺ 376.1404), 398.1223 (calculated for [(C₂₀H₁₇N₅O₃)Na]⁺ 398.1224). ¹H NMR (CDCl₃) δ 3.82 (s, 3H, OC*H₃*), 5.37 (s, 2H, C*H₂*), 6.51 (pseudo-t, 2.0 Hz, 2H, Pz *H⁴*), 6.93 (d, 2H, Ph *H³⁻⁵*), 7.42 (d, 2H, Ph *H²/⁶*), 7.78 (d, 1.8 Hz, 2H, Pz *H³*), 8.38 (s, 2H, Py *H³/⁵*), 8.55 (d, 2.6 Hz, 2H, Pz *H⁵*). ¹³C NMR (CDCl₃) δ 55.5 (O*C*H₃), 67.9 (1C, *C*H₂), 108.5 (2C, Pz *C⁴*), 109.4 (2C, Py *C³/⁵*), 114.2 (2C, Ph *C³/⁵*), 127.4 (2C, Pz *C⁵*), 127.4 (1C, Ph *C¹*), 130.8 (2C, Ph *C²/⁶*), 143.0 (2C, Pz *C³*), 143.6 (1C, Py *C⁴*), 150.9 (2C, Py *C²/⁶*), 160.1 (1C, Ph *C⁴*), 164.1 (1C, *C*OOR).

3.2.5. Synthesis of 3,4-dimethoxybenzyl 2,6-di(pyrazol-1-yl)pyridine-4-carboxylate (L⁷)

Method was as for L^5, using bpp^COOH (1.10 g, 4.31 mmol), DCC (1.96 g, 9.48 mmol), 3,4-dimethoxybenzyl alcohol (0.73 g, 4.31 mmol), and a catalytic amount of DMAP. The crude product was recrystallized from hot acetonitrile, affording a white polycrystalline powder. Yield: 1.20 g, 69%. Mp: 130–131 °C. HR-ES MS *m/z* 406.1507 (calculated for [(C₂₁H₁₉N₅O₄)H]⁺ 406.1510), 428.1335 (calculated for [(C₂₀H₁₇N₅O₃)Na]⁺ 428.1329), 833.2764 (calculated for [(C₂₀H₁₇N₅O₃)₂Na]⁺ 833.2766). ¹H NMR (CDCl₃) δ 3.78, 3.79 (both s, 3H, 2xOC*H₃*), 5.35 (s, 2H, C*H₂*), 6.65 (pseudo-t, 2.0 Hz, 2H, Pz *H⁴*), 7.01 (d, 1H, Ph *H⁵*), 7.07 (dd, 1H, Ph *H⁶*), 7.15 (d, 1H, Ph *H²*), 7.89 (d, 2H, Pz *H³*), 8.13 (s, 2H, Py *H³/⁵*), 8.96 (d, 2H, Pz *H⁵*). ¹³C NMR (CDCl₃) δ 55.5 (2C, 2xO*C*H₃), 67.7 (1C, *C*H₂), 107.8 (2C, Py *C³/⁵*), 108.9 (2C, Pz *C⁴*), 111.7 (1C, Ph *C²*), 112.7 (1C, Ph *C⁵*), 121.6 (2C, Ph *C⁶*), 127.4 (1C, Ph *C¹*), 128.4 (2C, Pz *C⁵*),

143.0 (1C, Py C^4), 143.2 (2C, Pz C^3), 148.7, 149.1 (both 1C, Ph C^3 and C^4), 150.4 (2C, Py $C^{2/6}$), 163.3 (1C, $COOR$).

3.2.6. Synthesis of [Fe(L^3)₂][BF₄]₂.

Filtered solutions of L^3 (39 mg, 0.10 mmol) and Fe[BF₄]₂·6H₂O (17 mg, 0.050 mmol) in nitromethane (7.5 cm³) were mixed at room temperature. The resultant solution was filtered and concentrated to ca. one-third its original volume. Slow diffusion of diethyl ether vapour into the solution yielded prismatic crystals of α-[Fe(L^3)₂][BF₄]₂·2CH₃NO₂, which were often contaminated by yellow plates of the β-[Fe(L^3)₂][BF₄]₂·2CH₃NO₂ polymorph. Yield: 32 mg, 63%. Found C, 47.3; H, 3.48; N, 13.6 %. Calculated for C₄₀H₃₄B₂F₈FeN₁₀O₈ C, 47.5; H, 3.39; N, 13.8%. ¹H NMR (CD₃CN) δ 3.90 (12H, OCH_3), 7.10 (6H; Ph H^2, H^5 and H^6), 23.2, 26.4 (both 4H, Pz H^3 and H^4), 39.6, 40.4 (both 4H, Pz H^5 and Py $H^{3/5}$).

3.2.7. Synthesis of [Fe(L^4)₂][BF₄]₂

Filtered solutions of L^4 (0.16 g, 0.46 mmol) and Fe[BF₄]₂·6H₂O (0.075 g, 0.22 mmol) in acetone (10 cm³) were mixed at room temperature. The resultant solution was filtered and concentrated to ca. one-third its original volume. Slow diffusion of diethyl ether vapour into the solution yielded the product as a dark red powder. Recrystallization from acetonitrile/diethyl ether afforded single crystals of the complex. While the crystal used for X-Ray analysis was apparently solvent-free, microanalysis of the bulk material was more consistent with a dihydrate formulation. Yield: 42 mg, 20%. Found C, 43.4; H, 2.59; N, 13.7%. Calculated for C₃₆H₂₆B₂F₈FeN₁₀O₈·2H₂O C, 43.6; H, 3.05; N, 14.1%. ¹H NMR (CD₃CN) δ 6.89 (2H), 6.99 (4H; Ph H^2, H^5 and H^6), 7.25, 7.37 (both br s, 2H, OH), 23.1, 26.0 (both 4H, Pz H^3 and H^4), 39.8, 40.3 (both 4H, Pz H^5 and Py $H^{3/5}$).

3.2.8. Synthesis of [Fe(L^5)₂][BF₄]₂

Method as for [Fe(L^4)₂][BF₄]₂, using L^5 (0.10 g, 0.27 mmol) and Fe[BF₄]₂·6H₂O (0.55 g, 0.14 mmol) in acetone (6 cm³). Crystals of the product obtained from the reaction mixture were well formed but diffracted poorly. Recrystallization of the complex from acetonitrile/diethyl ether yielded solvate crystals [Fe(L^5)₂][BF₄]₂·3/2CH₃CN, which were suitable for crystallographic characterization. Yield: 0.097 g, 75%. Found C, 49.5; H, 3.17; N, 15.1%. Calculated for C₃₈H₃₀B₂F₈FeN₁₀O₄ C, 49.6; H, 3.29; N, 15.2%. ¹H NMR (CD₃CN) δ 5.66 (4H, CH_2), 7.48 (2H, Ph H⁴), 7.54, 7.73 (both 4H, Ph $H^{2/6}$ and $H^{3/5}$), 20.2, 23.7 (both 4H, Pz H^3 and H^4), 35.4, 36.9 (both 4H, Pz H^5 and Py $H^{3/5}$).

3.2.9. Synthesis of [Fe(L^6)₂][BF₄]₂

Method as for [Fe(L^4)₂][BF₄]₂, using L^6 (0.10 g, 0.27 mmol) and Fe[BF₄]₂·6H₂O (0.50 g, 0.13 mmol). The red product was recrystallized from acetonitrile/diethyl ether for crystallographic characterization. Yield: 0.10 g, 78%. Found C, 48.9; H, 3.61; N, 14.1%. Calculated for C₄₀H₃₄B₂F₈FeN₁₀O₆ C, 49.0; H, 3.50; N, 14.3%. ¹H NMR (CD₃CN) δ 3.84 (6H, OCH_3), 5.57 (4H, CH_2), 7.07 and 7.64 (both 4H, Ph $H^{2/6}$ and $H^{3/5}$), 21.4, 24.9 (both 4H, Pz H^3 and H^4), 38.3, 40.1 (both 4H, Pz H^5 and Py $H^{3/5}$).

3.2.1.0 Synthesis of [Fe(L^7)₂][BF₄]₂

Method as for [Fe(L^4)₂][BF₄]₂, using L^7 (0.20 g, 0.49 mmol) and Fe[BF₄]₂·6H₂O (0.93 g, 0.25 mmol). Diffusion of diethyl ether vapour into the concentrated solution yielded red prismatic crystals. Yield: 0.10 g, 38%. Found C, 48.4; H, 3.72; N, 13.3%. Calculated for C₄₂H₃₈B₂F₈FeN₁₀O₈ C, 48.5; H, 3.68; N, 13.5%. ¹H NMR (CD₃CN) δ 3.86 (12H, OCH_3), 5.55 (4H, CH_2), 7.04 (2H), 7.26 (4H; Ph H^2, H^5 and H^6), 21.3, 24.7 (both 4H, Pz H^3 and H^4), 37.1 (8H, Pz H^5 and Py $H^{3/5}$).

3.3. Crystal structure determinations.

Experimental data for the crystal structures are listed in Tables 3 and 4. Diffraction data for L^5, L^6, and L^7·¹/₂MeCN were collected at station I19 of the Diamond synchrotron (λ = 0.6889 Å). The other

crystals were measured with an Agilent Supernova dual-source diffractometer using monochromated Cu-K_α (λ = 1.5418 Å) or Mo-K_α (λ = 0.7107 Å) radiation. The experimental details of the structures determinations in this study are given in Tables 3 and 4. All the structures were solved by direct methods (*SHELXS97* [60]), and developed by full least-squares refinement on F^2 (*SHELXL97* [60]). Crystallographic figures were prepared using *XSEED* [61], while the V_{Oh} FeN$_6$ coordination volumes were calculated using *OLEX2* [62].

CCDC-1884419 (L^3), CCDC-1884420 (L^5), CCDC-1884421 (L^6), CCDC-1884422 ($L^7 \cdot 1/2$MeCN), CCDC-1884423 (α-[Fe(L^3)$_2$][BF$_4$]$_2 \cdot 2$MeNO$_2$), CCDC-1884424 (β-[Fe(L^3)$_2$][BF$_4$]$_2 \cdot 2$MeNO$_2$), CCDC-1884425 ([Fe(L^4)$_2$][BF$_4$]$_2$), CCDC-1884426 ([Fe(L^5)$_2$][BF$_4$]$_2 \cdot 3/2$MeCN), and CCDC-1884427 ([Fe(L^6)$_2$][BF$_4$]$_2 \cdot 3/2$MeCN) contain the supplementary crystallographic data for this paper. These data can be obtained free of charge from The Cambridge Crystallographic Data Centre via www.ccdc.cam.ac.uk/data_request/cif.

Table 3 Experimental details for the organic ligand crystal structures in this work.

Compound	L^3	L^5	L^6	$L^{7} \cdot 1/2$MeCN
formula	$C_{20}H_{17}N_5O_4$	$C_{19}H_{15}N_5O_2$	$C_{20}H_{17}N_5O_3$	$C_{22}H_{20.5}N_{5.5}O_4$
M_r	391.39	345.36	375.39	425.94
crystal class	monoclinic	monoclinic	orthorhombic	monoclinic
space group	$P2_1/c$	Pc	$Pbca$	$P2_1/c$
a / Å	11.9677(2)	7.2833(1)	42.4116(3)	8.0803(1)
b / Å	20.7834(4)	7.7290(1)	11.4438(1)	65.5346(6)
c / Å	7.3138(1)	29.9811(5)	7.2071(1)	7.6027(1)
β / °	90.900(2)	92.924(1)	–	91.061(1)
V / Å^3	1818.93(5)	1685.52(4)	3497.96(6)	4025.24(8)
Z	4	4	8	8
T / K	120(2)	100(2)	100(2)	100(2)
D_{calcd} / Mgm^{-3}	1.429	1.361	1.426	1.406
μ / mm^{-1}	0.855[a]	0.093[b]	0.100[b]	0.100[b]
measured reflections	7444	25320	50109	62089
unique reflections	3524	7820	8534	18798
observed reflections	3020	4902	6291	12124
R_{int}	0.026	0.102	0.091	0.056
R_1 [$Fo > 4\sigma(Fo)$][c]	0.042	0.070	0.054	0.063
wR_2 [all data][d]	0.113	0.192	0.162	0.174
GoF	1.038	0.992	1.021	1.034
Flack parameter	–	–0.5(12)[e]	–	–
$\Delta\rho$max, $\Delta\rho$min / eÅ^{-3}	0.31/–0.21	0.34/–0.44	0.80/–0.35	0.56/–0.42

[a] Collected with Cu-K_α radiation; [b] Collected with synchrotron radiation; [c] $R = \Sigma[|F_o| - |F_c|] / \Sigma|F_o|$; [d] $wR = [\Sigma w(F_o^2 - F_c^2) / \Sigma wF_o^4]^{1/2}$; [e] The absolute structure of this light-atom crystal could not be determined.

Unless otherwise stated, all crystallographically ordered non-H atoms in the structures described below were refined anisotropically, and H atoms were placed in calculated positions and refined using a riding model. Disordered BF$_4^-$ ions were modelled using refined B–F and F…F distance restraints, while fixed distance restraints were applied to disordered solvent molecules.

3.3.1. Organic ligand crystallographic refinements.

The asymmetric unit of L^5 contains two unique molecules of the compound while that of $L^{7} \cdot 1/2$MeCN contains two molecules of L^7 and one acetonitrile molecule. All the H atoms in L^3, L^6, and $L^{7} \cdot 1/2$MeCN were located in the Fourier map and refined positionally, with U_{iso} constrained to 1.5x U_{eq} of the corresponding C atom for methyl group H atoms, or to 1.2x U_{eq}\{C\} for other H atoms. H atom positions were not refined for L^5, because of the lower data:parameter ratio in that refinement.

While the L^5 crystal adopts a handed space group, its absolute structure could not be unambiguously determined owing to its light atom composition. Hence, the Friedel opposite reflections in this dataset were merged for the final least squares refinement cycles.

Table 4 Experimental details for the metal complex crystal structures in this work.

Compound	α-[Fe(L^3)$_2$][BF$_4$]$_2$·2MeNO$_2$	β-[Fe(L^3)$_2$][BF$_4$]$_2$·2MeNO$_2$	[Fe(L^4)$_2$][BF$_4$]$_2$
formula	C$_{42}$H$_{40}$B$_2$F$_8$FeN$_{12}$O$_{12}$	C$_{42}$H$_{40}$B$_2$F$_8$FeN$_{12}$O$_{12}$	C$_{36}$H$_{26}$B$_2$F$_8$FeN$_{10}$O$_8$
M_r	1134.33	1134.33	956.14
crystal class	triclinic	triclinic	triclinic
space group	$P\bar{1}$	$P\bar{1}$	$P\bar{1}$
a / Å	8.3230(2)	11.3601(9)	8.6675(3)
b / Å	12.8302(2)	13.2652(13)	16.8378(6)
c / Å	23.1765(6)	17.5490(15)	27.0770(11)
α / °	88.116(2)	67.671(9)	85.102(3)
β / °	80.270(2)	80.155(7)	82.500(3)
γ / °	89.567(2)	78.463(8)	87.451(3)
V / Å^3	2438.00(9)	2383.6(4)	3901.3(3)
Z	2	2	4
T / K	120(2)	120(2)	120(2)
D_{calcd} / Mgm^{-3}	1.545	1.580	1.628
μ / mm^{-1}	3.412[a]	3.490[a]	4.048[a]
measured reflections	42688	18126	59552
unique reflections	9491	8979	15161
observed reflections	9123	6467	10540
R_{int}	0.035	0.065	0.075
R_1 [$Fo>4\sigma(Fo)$][c]	0.048	0.068	0.073
wR_2 [all data][d]	0.134	0.186	0.218
GoF	1.066	1.049	1.030
$\Delta\rho$max, $\Delta\rho$min / eÅ^{-3}	1.30/−0.85	0.71/−0.84	0.85/−0.61
Compound	**[Fe(L^5)$_2$][BF$_4$]$_2$·3/2MeCN**	**[Fe(L^6)$_2$][BF$_4$]$_2$·3/2MeCN**	
formula	C$_{41}$H$_{34.5}$B$_2$F$_8$FeN$_{11.5}$O$_4$	C$_{43}$H$_{38.5}$B$_2$F$_8$FeN$_{11.5}$O$_6$	
M_r	981.77	1041.82	
crystal class	triclinic	monoclinic	
space group	$P\bar{1}$	$P2_1/c$	
a / Å	13.8965(6)	27.4401(4)	
b / Å	17.0836(7)	16.5615(3)	
c / Å	20.8001(7)	20.5281(2)	
α / °	95.020(3)	−	
β / °	102.703(3)	100.257(1)	
γ / °	113.133(4)	−	
V / Å^3	4345.8(3)	9179.9(2)	
Z	4	8	
T / K	150(2)	150(2)	
D_{calcd} / Mgm^{-3}	1.501	1.508	
μ / mm^{-1}	0.438[b]	3.466[a]	
measured reflections	46531	77065	
unique reflections	20799	17911	
observed reflections	13895	15370	
R_{int}	0.037	0.051	
R_1 [$Fo>4\sigma(Fo)$][c]	0.067	0.080	
wR_2 [all data][d]	0.170	0.220	
GoF	1.032	1.033	
$\Delta\rho$max, $\Delta\rho$min / eÅ^{-3}	1.02/−0.59	1.25/−0.97	

[a] Collected with Cu-K_α radiation. [b] Collected with Mo-K_α radiation. [c] $R = \Sigma[|F_o| - |F_c|] / \Sigma|F_o|$.

[d] $wR = [\Sigma w(F_o^2 - F_c^2) / \Sigma w F_o^4]^{1/2}$.

3.3.2. Crystallographic refinement of α-[Fe(L^3)$_2$][BF$_4$]$_2$·2MeNO$_2$

One of the BF$_4$$^-$ ions is disordered over two sites, with refined occupancies of 0.59:0.41. One nitromethane molecule is also disordered, and was refined over two orientations with the same

occupancy ratio, but shares a common wholly occupied N atom. The highest residual Fourier peak of +1.3 eÅ^{-3} lies within the disordered anion.

3.3.3. Crystallographic refinement of β-[Fe(L³)₂][BF₄]₂·2MeNO₂

One of the BF₄⁻ ions is disordered over three equally populated sites.

3.3.4. Crystallographic refinement of [Fe(L⁴)₂][BF₄]₂

The asymmetric unit contains two crystallographically unique complex dications labelled 'A' and 'B'; three whole BF₄⁻ anions; and, two BF₄⁻ half-anion sites close to crystallographic inversion centres. The dihydroxyphenyl substituent C(48B)-O(55B) is badly disordered and was refined over three sites with occupancies of 0.5:0.25:0.25 (the *C*3-hydroxyl O atom in orientation 'D' is further disordered over two equally occupied sites). These disordered phenyl groups were refined as rigid hexagons and with the fixed restraint C–O = 1.37(2) Å. One of the whole BF₄⁻ ions, and both of the half-anions, are also disordered over two or three sites.

3.3.5. Crystallographic refinement of [Fe(L⁵)₂][BF₄]₂·³/₂MeCN

The asymmetric unit contains two unique complex dications, four BF₄⁻ anions and three molecules of acetonitrile. One benzyl substituent in each complex molecule was refined as disordered, both over two sites with a 0.6:0.4 occupancy ratio. The partial phenyl groups associated with this disorder were refined as rigid hexagons. Two of the anions are also disordered, one over two equally occupied sites and the other over three orientations with occupancies 0.60, 0.15, and 0.25; the first two of these share a common 0.75-occupied B atom. All fully occupied non-H atoms, plus F atoms with occupancy ≥0.5, were refined anisotropically.

3.3.6. Crystallographic refinement of [Fe(L⁶)₂][BF₄]₂·³/₂MeCN

The asymmetric unit of this crystal also contains two formula units of the compound. That is, two complex dications, four BF₄⁻ anions, and three molecules of acetonitrile. Two of the anions are disordered, one over two equally occupied sites and the other over two orientations by rotation about a B–F bond with occupancies of 0.75 and 0.25. The highest residual Fourier peak of +1.3 eÅ^{-3} lies within one of the disordered anions.

4. Conclusions

Five new phenyl or benzyl 2,6-di(pyrazol-1-yl)pyridine-4-carboxylate esters have been synthesized and complexed to iron(II). The two polymorphs α- and β-[Fe(L³)₂][BF₄]₂·2MeNO₂ are noteworthy as rare examples of high-spin and low-spin polymorphs of the same iron complex [63]. This reflects the presence of similar populations of both spin states in solutions of the complex at room temperature (Figure 7) which, unusually, crystallize as separate crystal forms. The β–polymorph is trapped in its high-spin state by its twisted coordination geometry, which is significantly distorted from idealized *D*₂d symmetry. While that is a common feature of high-spin [Fe(bpp)₂]²⁺ derivatives [24], the separate crystallization of weakly distorted low-spin and strongly distorted high-spin polymorphs of the same complex has only been observed once before in this metal/ligand system [64].

The spin state properties of α-[Fe(*L*³)₂][BF₄]₂·2MeNO₂ and most of the other complexes in this work resemble those of [Fe(*L*¹)₂][BF₄]₂, [Fe(*L*²)₂][BF₄]₂ [43] and other iron complexes of 2,6-di(pyrazol-1-yl)pyridine-4-carboxylate ester ligands [29,37,44–46]. That is, they are fully or predominantly low-spin at lower temperature but show the onset of gradual SCO on warming past room temperature. The exception is [Fe(*L*⁵)₂][BF₄]₂, which exhibits a more abrupt, hysteretic spin-transition near room temperature after recrystallization from acetone solution. Although this phase was not crystallographically characterised, it indicates that more cooperative SCO switching can be obtained with benzyl 2,6-di(pyrazol-1-yl)pyridine-4-carboxylate esters compared to their phenyl ester counterparts.

A feature of the crystal structures in this work is the regular occurrence of two unique molecules in the crystallographic asymmetric units. Thus, the crystal structures of L^5, $L^{7\cdot1}/2$MeCN, and all the complexes [FeL_2][BF$_4$]$_2$ ($L = L^4$-L^7) exhibit $Z' = 2$. The structure of [Fe(L^4)$_2$][BF$_4$]$_2$ is distinct from the others since the feature distinguishing its two unique complex cations is the presence or absence of sterically imposed disorder of a phenyl ester substituent. In the other cases, the crystallographically unique molecules show the presence or absence of ligand disorder to a similar extent but often differ in the conformations in their benzyl ester substituents. That implies the added flexibility of benzyl methylene linker in L^5–L^7 contributes to this structural complexity. Be that as it may, there is clear potential for novel SCO structure:function properties in the iron/benzyl 2,6-di(pyrazol-1-yl)pyridine-4-carboxylate system which we are continuing to pursue in our current work.

References

1. Gütlich, P.; Goodwin, H.A. (eds.) *Spin Crossover in Transition Metal Compounds I-III. Topics in Current Chemistry vols. 233–235*; Springer, Berlin, Germany, 2004.

2. Halcrow, M.A. (ed.) *Spin-Crossover Materials—Properties and Applications*; John Wiley & Sons: Chichester, UK, 2013; p. 568.

3. Kumar, K.S.; Ruben, M. Emerging trends in spin crossover (SCO) based functional materials and devices. *Coord. Chem. Rev.* **2017**, *346*, 176−205.

4. Kahn, O.; Kröber, J.; Jay, C. Spin transition molecular materials for displays and data recording. *Adv. Mater.* **1992**, *4*, 718−728.

5. Manrique-Juárez, M.D.; Rat, S.; Salmon, L.; Molnár, G.; Quintero, C.M.; Nicu, L.; Shepherd, H.J.; Bousseksou, A. Switchable molecule-based materials for micro- and nanoscale actuating applications: Achievements and prospects. *Coord. Chem. Rev.* **2016**, *308*, 395−408.

6. Zhang, X.; Mu, S.; Chastanet, G.; Daro, N.; Palamarciuc, T.; Rosa, P.; Létard, J.-F.; Liu, J.; Sterbinsky, G.E.; Arena, D.A.; et al. Complexities in the molecular spin crossover transition. *J. Phys. Chem. C* **2015**, *119*, 16293−16302.

7. Bovo, G.; Braunlich, I.; Caseri, W.R.; Stingelin, N.; Anthopoulos, T.D.; Sandeman, K.G.; Bradley, D.D.C.; Stavrinou, P.N. Room temperature dielectric bistability in solution-processed spin crossover polymer thin films. *J. Mater. Chem. C* **2016**, *4*, 6240−6248.

8. Rat, S.; Piedrahita-Bello, M.; Salmon, L.; Molnár, G.; Demont, P.; Bousseksou, A. Coupling mechanical and electrical properties in spin crossover polymer composites. *Adv. Mater.* **2018**, *30*, 1705275.

9. Diaconu, A.; Lupu, S.-L.; Rusu, I.; Risca, I.-M.; Salmon, L.; Molnár, G.; Bousseksou, A.; Demont, P.; Rotaru, A. Piezoresistive effect in the [Fe(Htrz)$_2$(trz)](BF$_4$) spin crossover complex *J. Phys. Chem. Lett.* **2017**, *8*, 3147−3151.

10. Phan, H.; Benjamin, S.M.; Steven, E.; Brooks, J.S.; Shatruk, M. Photomagnetic response in highly conductive iron(II) spin-crossover complexes with TCNQ radicals. *Angew. Chem. Int. Ed.* **2015**, *54*, 823−827.

11. Shvachko, Y.N.; Starichenko, D.V.; Korolyov, A.V.; Yagubskii, E.B.; Kotov, A.I.; Buravov, L.I.; Lyssenko, K.A.; Zverev, V.N.; Simonov, S.V.; Zorina, L.V.; et al. The conducting spin-crossover compound combining Fe(II) cation complex with TCNQ in a fractional reduction state. *Inorg. Chem.* **2016**, *55*, 9121−9130.

12. Wang, H.-Y.; Ge, J.-Y.; Hua, C.; Jiao, C.-Q.; Wu, Y.; Leong, C.F.; D'Alessandro, D.M.; Liu, T.; Zuo, J.-L. Photo- and electronically switchable spin-crossover iron(II) metal-organic frameworks based on a tetrathiafulvalene ligand. *Angew. Chem. Int. Ed.* **2017**, *56*, 5465−5470.

13. Lochenie, C.; Schötz, K.; Panzer, F.; Kurz, H.; Maier, B.; Puchtler, F.; Agarwal, S.; Köhler, A.; Weber, B. Spin-crossover iron(II) coordination polymer with fluorescent properties: Correlation between emission properties and spin state. *J. Am. Chem. Soc.* **2018**, *140*, 700–709.

14. Yuan, J.; Wu, S.-Q.; Liu, M.-J.; Sato, O.; Kou, H.-Z. Rhodamine 6G-labeled pyridyl aroylhydrazone Fe(II) complex exhibiting synergetic spin crossover and fluorescence. *J. Am. Chem. Soc.* **2018**, *140*, 9426–9433.

15. Wang, J.-Li.; Liu, Q.; Meng, Y.-S.; Liu, X.; Zheng, H.; Shi, Q.; Duan, C.-Y.; Liu, T. Fluorescence modulation via photoinduced spin crossover switched energy transfer from fluorophores to Fe^{II} ions. *Chem. Sci.* **2018**, *9*, 2892–2897.

16. Gaspar, A.B.; Seredyuk, M. Spin crossover in soft matter. *Coord. Chem. Rev.* **2014**, *268*, 41–58.

17. Kuroiwa, K. Supramolecular control of spin crossover phenomena using various amphiphiles. *Inorganics* **2017**, *5*, 45.

18. Salmon, L.; Catala, L. Spin-crossover nanoparticles and nanocomposite materials. *C. R. Chim.* **2018**, *21*, 1230–1269.

19. Mallah, T.; Cavallini, M. Surfaces, thin films and patterning of spin crossover compounds. *C. R. Chim.* **2018**, *21*, 1270–1286.

20. Mikolasek, M.; Felix, G.; Nicolazzi, W.; Molnár, G.; Salmon, L.; Bousseksou, A. Finite size effects in molecular spin crossover materials. *New J. Chem.* **2014**, *38*, 1834–1839.

21. Molnár, G.; Rat, S.; Salmon, L.; Nicolazzi, W.; Bousseksou, A. Spin crossover nanomaterials: From fundamental concepts to devices. *Adv. Mater.* **2018**, *30*, 1703862.

22. Halcrow, M.A. Iron(II) complexes of 2,6-di(pyrazol-1-yl)pyridines—A versatile system for spin-crossover research. *Coord. Chem. Rev.* **2009**, *253*, 2493–2514.

23. Olguín, J.; Brooker, S. Spin crossover active iron(II) complexes of selected pyrazole-pyridine/pyrazine ligands. *Coord. Chem. Rev.* **2011**, *255*, 203–240.

24. Kershaw Cook, L.J.; Mohammed, R.; Sherborne, G.; Roberts, T.D.; Alvarez, S.; Halcrow, M.A. Spin state behaviour of iron(II)/dipyrazolylpyridine complexes. New insights from crystallographic and solution measurements. *Coord. Chem. Rev.* **2015**, *289–290*, 2–12.

25. Halcrow, M.A. Recent advances in the synthesis and applications of 2,6-dipyrazolylpyridine derivatives and their complexes, *New J. Chem.* **2014**, *38*, 1868–1882.

26. Holland, J.M.; Barrett, S.A.; Kilner, C.A.; Halcrow, M.A. Control of the spin state of Fe(II) 2,6-di(pyrazol-1-yl)pyridine complexes by distal ligand substitution. *Inorg. Chem. Commun.* **2002**, *5*, 328–332.

27. Kershaw Cook, L.J.; Kulmaczewski, R.; Mohammed, R.; Dudley, S.; Barrett, S.A.; Little, M.A.; Deeth, R.J.; Halcrow, M.A. A unified treatment of the relationship between ligand substituents and spin state in a family of iron(II) complexes. *Angew. Chem. Int. Ed.* **2016**, *55*, 4327–4331.

28. González-Prieto, R.; Fleury, B.; Schramm, F.; Zoppellaro, G.; Chandrasekar, R.; Fuhr, O.; Lebedkin, S.; Kappes, M.; Ruben, M. Tuning the spin-transition properties of pyrene-decorated 2,6-bispyrazolylpyridine based Fe(II) complexes. *Dalton Trans.* **2011**, *40*, 7564–7570.

29. Kumar, K.S.; Šalitroš, I.; Moreno-Pineda, E.; Ruben, M. Spacer type mediated tunable spin crossover (SCO) characteristics of pyrene decorated 2,6-bis(pyrazol-1-yl)pyridine (bpp) based Fe(II) molecular spintronic modules. *Dalton Trans.* **2017**, *46*, 9765–9768.

30. Santoro, A.; Kershaw Cook, L.J.; Kulmaczewski, R.; Barrett, S.A.; Cespedes, O.; Halcrow, M.A. Iron(II) complexes of tridentate indazolylpyridine ligands: Enhanced spin-crossover hysteresis and ligand-based fluorescence. *Inorg. Chem.* **2015**, *54*, 682–693.

31. Schäfer, B.; Bauer, T.; Faus, I.; Wolny, J.A.; Dahms, F.; Fuhr, O.; Lebedkin, S.; Wille, H.-C.; Schlage, K.; Chevalier, K.; et al. A luminescent Pt₂Fe spin crossover complex. *Dalton Trans.* **2017**, *46*, 2289–2302.

32. Hasegawa, Y.; Sakamoto, R.; Takahashi, K.; Nishihara, H. Solid-state ligand-driven light-induced spin change at ambient temperatures in bis(dipyrazolylstyrylpyridine)iron(II) complexes. *Inorg. Chem.* **2013**, *52*, 1658–1665.

33. Nihei, M.; Han, L.; Oshio, H. Magnetic bistability and single-crystal-to-single-crystal transformation induced by guest desorption. *J. Am. Chem. Soc.* **2007**, *129*, 5312–5313.

34. Nihei, M.; Takahashi, N.; Nishikawa, H.; Oshio, H. Spin-crossover behavior and electrical conduction property on iron(II) complexes with tetrathiafulvalene moieties. *Dalton Trans.* **2011**, *40*, 2154–2156.

35. Abhervé, A.; Palacios-Corella, M.; Clemente-Juan, J.M.; Marx, R.; Neugebauer, P.; van Slageren, J.; Clemente-León, M.; Coronado, E. Bimetallic Mn^{III}–Fe^{II} hybrid complexes formed by a functionalized Mn^{III} Anderson polyoxometalate coordinated to Fe^{II}: Observation of a field-induced slow relaxation of magnetization in the Mn^{III} centres and a photoinduced spin-crossover in the Fe^{II} centres. *J. Mater. Chem. C* **2015**, *3*, 7936−7945.

36. Abhervé, A.; Recio-Carretero, M.J.; López-Jordà, M.; Clemente-Juan, J.M.; Canet-Ferrer, J.; Cantarero, A.; Clemente-León, M.; Coronado, E. Nonanuclear spin-crossover complex containing iron(II) and iron(III) based on a 2,6-bis(pyrazol-1-yl)pyridine ligand functionalized with a carboxylate group. *Inorg. Chem.* **2016**, *55*, 9361–9367.

37. Rajadurai, C.; Fuhr, O.; Kruk, R.; Ghafari, M.; Hahn, H.; Ruben, M. Above room temperature spin transition in a metallo-supramolecular coordination oligomer/polymer. *Chem. Commun.* **2007**, 2636−2638.

38. Tovee, C.A.; Kilner, C.A.; Barrett, S.A.; Thomas, J.A.; Halcrow, M.A. A back-to-back ligand with dipyrazolylpyridine and dipicolylamine metal-binding domains. *Eur. J. Inorg. Chem.* **2010**, 1007−1012.

39. Kershaw Cook, L.J.; Fisher, J.; Harding, L.P.; Halcrow, M.A. An iron(II) spin-crossover metallacycle from a back-to-back bis-[dipyrazolylpyridine]. *Dalton Trans.* **2015**, *44*, 9417−9425.

40. Devid, E.J.; Martinho, P.N.; Kamalakar, M.V.; Šalitroš, I.; Prendergast, U.; Dayen, J.-F.; Meded, V.; Lemma, T.; González-Prieto, R.; Evers, F.; et al. Spin transition in arrays of gold nanoparticles and spin crossover molecules. *ACS Nano* **2015**, *9*, 4496–4507.

41. Pukenas, L.; Benn, F.; Lovell, E.; Santoro, A.; Kershaw Cook, L.J.; Halcrow, M.A.; Evans, S.D. Bead-like structures and self-assembled monolayers from 2,6-dipyrazolylpyridines and their iron(II) complexes. *J. Mater. Chem. C* **2015**, *3*, 7890−7896.

42. Kumar, K.S.; Šalitroš, I.; Boubegtiten-Fezoua, Z.; Moldovan, S.; Hellwig, P.; Ruben, M. A spin crossover (SCO) active graphene-iron(II) complex hybrid material. *Dalton Trans.* **2018**, *47*, 35−40.

43. Galadzhun, I.; Kulmaczewski, R.; Cespedes, O.; Yamada, M.; Yoshinari, N.; Konno, T.; Halcrow, M.A. 2,6-Di(pyrazolyl)pyridine-4-carboxylate esters with alkyl chain substituents, and their iron(II) complexes. *Inorg. Chem.* **2018**, *57*, 13761–13771.

44. Bridonneau, N.; Rigamonti, L.; Poneti, G.; Pinkowicz, D.; Forni, A.; Cornia, A. Evidence of crystal packing effects in stabilizing high or low spin states of iron(II) complexes with functionalized 2,6-bis(pyrazol-1-yl)pyridine ligands. *Dalton Trans.* **2017**, *46*, 4075–4085.

45. García-López, V.; Palacios-Corella, M.; Abhervé, A.; Pellicer-Carreño, I.; Desplanches, C.; Clemente-León, M.; Coronado, E. Spin-crossover compounds based on iron(II) complexes of 2,6-bis(pyrazol-1-yl)pyridine (bpp) functionalized with carboxylic acid and ethyl carboxylic acid. *Dalton Trans.* **2018**, *47*, 16958–16968.

46. Kumar, K.S.; Šalitroš, I.; Suryadevara, N.; Moreno-Pineda, E.; Ruben, M. Supramolecular interaction tuning of spin-crossover in pyrene/fullerene (C$_{60}$) tethered Fe^{II}-2,6-di(pyrazol-1-yl)pyridine complexes: Towards switchable molecular devices. *Eur. J. Inorg. Chem.* **2018**, *2018*, 5091–5097.

47. Vermonden, T.; Branowska, D.; Marcelis, A.T.M.; Sudhölter, E.J.R. Synthesis of 4-functionalized terdendate pyridine-based ligands. *Tetrahedron* **2003**, *59*, 5039–5045.

48. Halcrow, M.A. The synthesis and coordination chemistry of 2,6-bis(pyrazolyl)pyridines and related ligands—Versatile terpyridine analogues. *Coord. Chem. Rev.* **2005**, *249*, 2880–2908.

49. Bessel, C.A.; See, R.F.; Jameson, D.L.; Churchill, M.R.; Takeuchi, K.J. Structural considerations of terdentate ligands: Crystal structures of 2,2':6',2''-terpyridine and 2,6-bis(pyrazol-1-yl)pyridine. *J. Chem. Soc. Dalton Trans.* **1992**, 3223–3228.

50. Guionneau, P.; Marchivie, M.; Bravic, G.; Létard, J.-F.; Chasseau, D. Structural aspects of spin crossover. example of the [Fe^{II}L$_n$(NCS)$_2$] complexes. *Top. Curr. Chem.* **2004**, *234*, 97−128.

51. Holland, J.M.; McAllister, J.A.; Kilner, C.A.; Thornton-Pett, M.; Bridgeman, A.J.; Halcrow, M.A. Stereochemical effects on the spin state transition shown by salts of [FeL$_2$]$^{2+}$ [L = 2,6-di(pyrazol-1-yl)pyridine]. *J. Chem. Soc. Dalton Trans.* **2002**, 548−554.

52. Vela, S.; Novoa, J.J.; Ribas-Arino, J. Insights into the crystal-packing effects on the spin crossover of [Fe^{II}(1-bpp)$_2$]$^{2+}$-based materials. *Phys. Chem. Chem. Phys.* **2014**, *16*, 27012−27024.

53. Kershaw Cook, L.J.; Thorp-Greenwood, F.L.; Comyn, T.P.; Cespedes, O.; Chastanet, G.; Halcrow, M.A. Unexpected spin-crossover and a low pressure phase change in an iron(II)/ dipyrazolylpyridine complex exhibiting a high-spin Jahn-Teller distortion. *Inorg. Chem.* **2015**, *54*, 6319−6330.

54. McCusker, J.K.; Rheingold, A.L.; Hendrickson, D.N. Variable-temperature studies of laser-initiated $^5T_2 \rightarrow$ $^1A_1$ intersystem crossing in spin-crossover complexes: Empirical correlations between activation parameters and ligand structure in a series of polypyridyl ferrous complexes. *Inorg. Chem.* **1996**, *35*, 2100–2112.

55. Capel Berdiell, I.; Kulmaczewsk, R.; Halcrow, M.A. Iron(II) complexes of 2,4-dipyrazolyl-1,3,5-triazine derivatives—The influence of ligand geometry on metal ion spin state. *Inorg. Chem.* **2017**, *56*, 8817–8828.

56. O'Connor, C.J. Magnetochemistry—Theory and experimentation. *Prog. Inorg. Chem.* **1982**, *29*, 203–283.

57. Evans, D.F. The determination of the paramagnetic susceptibility of substances in solution by nuclear magnetic resonance. *J. Chem. Soc.* **1959**, 2003–2005.

58. Schubert, E.M. Utilizing the Evans method with a superconducting NMR spectrometer in the undergraduate laboratory. *J. Chem. Educ.* **1992**, *69*, 62.

59. García, B.; Ortega, J.C. Excess viscosity η^E, excess volume V^E and excess free energy of activation ΔG^{*E} at 283, 293, 303, 313, and 323 K for mixtures of acetonitrile and alkyl benzoates. *J. Chem. Eng.* Data **1988**, *33*, 200–204.

60. Sheldrick, G.M. Crystal structure refinement with *SHELXL. Acta Crystallogr., Sect. C: Struct. Chem.* **2015**, *71*, 3–8.

61. Barbour, L.J. X-Seed—A software tool for supramolecular crystallography. *J. Supramol. Chem.* **2001**, *1*, 189–191.

62. Dolomanov, O.V.; Bourhis, L.J.; Gildea, R.J.; Howard, J.A.K.; Puschmann, H. OLEX2: A complete structure solution, refinement and analysis program. *J. Appl. Crystallogr.* **2009**, *42*, 339–341.

63. Tao, J.; Wei, R.-J.; Huang, R.-B.; Zheng, L.-S. Polymorphism in spin-crossover systems. *Chem. Soc. Rev.* **2012**, *41*, 703–737.

64. Haryono, M.; Heinemann, F.W.; Petukhov, K.; Gieb, K.; Müller, P.; Grohmann, A. Parallel crystallization of a "static" and a spin-crossover polymorph of an iron(II) complex from the same solution. *Eur. J. Inorg. Chem.* **2009**, 2136–2143.